Research Square

Preprints are preliminary reports that have not undergone peer review.
They should not be considered conclusive, used to inform clinical practice,
or referenced by the media as validated information.

Climate-informed stress tests expose hidden high-risk ports in the global shipping network

Zengkai Zhang

zengkaizhang@xmu.edu.cn

Xiamen University

Jianke Guo

Liaoning Normal University https://orcid.org/0000-0002-8463-921X

Yichuan Zhang

Liaoning Normal University

Article

Keywords:

Posted Date: August 11th, 2026

DOI: https://doi.org/10.21203/rs.3.rs-10468653/v1

License: This work is licensed under a Creative Commons Attribution 4.0 International License.
Read Full License

Additional Declarations: There is **NO** Competing Interest.

Climate-informed stress tests expose hidden high-risk ports in the global shipping network

Abstract

The global shipping network carries over 80% of global freight volumes, yet the systemic threat of multi-hazard climate risks to this critical infrastructure has not been quantified at the network level. Here, we integrate sea-level, sea-ice, and tropical cyclone data to construct the Global Maritime Shipping Climate Risk (GMSC-R) model, and introduce a natural attack strategy—a climate-informed stress test in which ports fail in descending order of climate vulnerability. We find that removing the most climate-vulnerable 66.7% of ports erases 96.4% (2017) and 79.0% (2021) of network efficiency, with the critical thresholds of degradation advancing substantially between the two years. Port climate risk concentrates in Asia and Europe; sea-level rise dominates the high-risk core zone (64.0% of ports in 2021, up from 57.5%), and the sea-ice-dominated share of this zone nearly doubled to 27.2%, signalling cumulative and diversifying threats. Against conventional topological attacks, our stress tests show that climate risk decouples from network centrality: Port Said overtakes Singapore, the most central hub, in the 2021 ranking, and a quarter of the hundred earliest-failing ports are invisible to centrality-guided screening. Our findings underscore the urgency of integrating multi-hazard climate risk into port planning and supply chain resilience.

Introduction

The global shipping network (GSN) carries over 80% of global freight volumes and serves as the physical backbone of international trade[1], playing a critical role in sustaining global economic

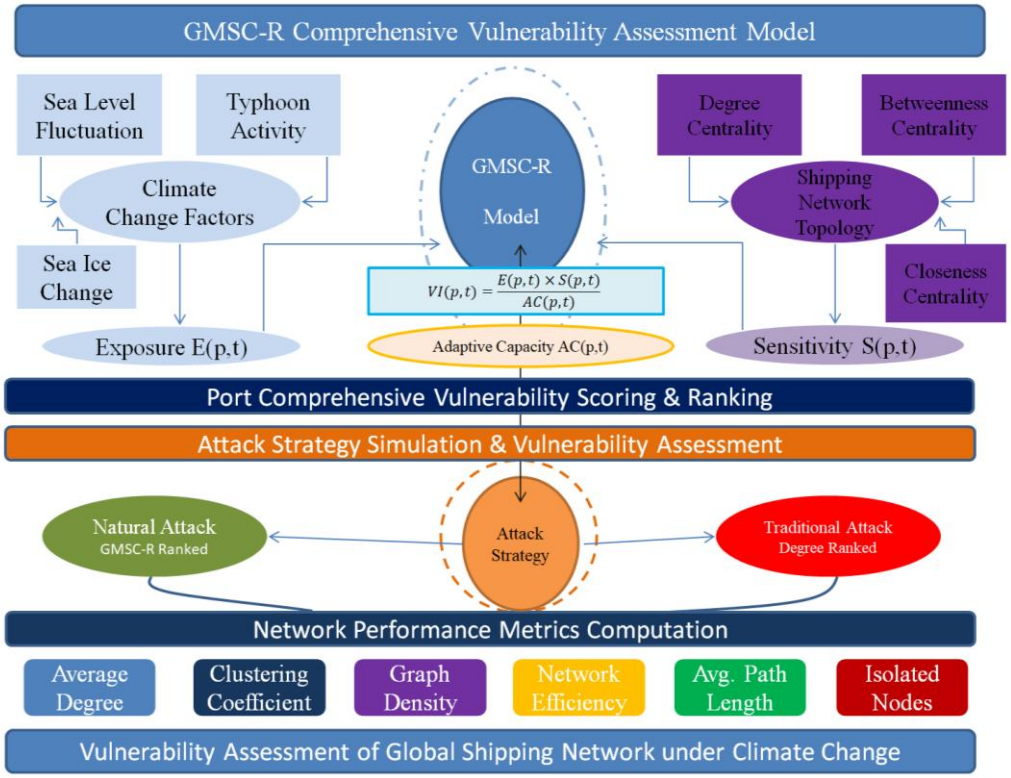
integration and supply chain resilience[2]. However, climate change is posing an increasingly severe, compounding threat to this critical infrastructure through multiple pathways[3-5]. Sea-level rise exacerbates inundation and storm surge risks at low-lying ports, potentially causing severe physical damage and prolonged operational disruption[6-8]. Arctic sea-ice retreat, while potentially opening new shipping routes[9-13], is accompanied by navigational hazards, infrastructure deficiencies, and geopolitical complexity[14-17]. Intensifying tropical cyclones directly damage port facilities and trigger systemic delays through network connectivity[18-20]. These climate-driven port disruptions can readily propagate through the topological connections of the GSN, triggering cascading failures that threaten global trade and supply chain stability [21-23]. Given the projected growth in maritime trade and escalating climate risks, a systematic assessment of port climate vulnerability at the global network level has become imperative[24].

Complex network theory has been widely applied to characterise GSN topology[25-27], revealing scale-free degree distributions[28,29] and small-world properties[30], with subsequent work incorporating temporal dynamics[31,32], edge weights[33], and multi-layer network representations[34,35]. In vulnerability assessment, common approaches simulate node or edge removal and measure the degradation of network efficiency, connectivity, or average path length[36-39]. However, existing research falls short in two key dimensions. On the one hand, mainstream attack strategies—whether random failures or targeted attacks based on degree or betweenness centrality[40-43]—inherently rely on purely topological indicators and struggle to capture the spatial heterogeneity, physical process complexity, and multi-hazard compounding effects characteristic of climate drivers[44,45]. On the other hand, conventional climate impact assessments are largely confined to single hazards or single regions, lacking a global-scale, multi-hazard, network-level perspective[46,47]. Moreover, existing GSN characterisation studies suffer

from significant data coverage limitations—most analyses encompass only a few hundred ports or specific regions[48-50]—falling short of supporting a truly global-scale systemic network assessment. There is therefore an urgent need for a new research paradigm that integrates multiple climate-related impacts and evaluates their combined effects at the network level.

To bridge these gaps, this study develops an integrated assessment framework. First, we integrate multi-source climate data on sea-level variability, sea-ice change, and tropical cyclone activity to construct the Global Maritime Shipping Climate Risk (GMSC-R) model. The model synthesises three dimensions—the physical climate exposure (Exposure) faced by a port, its topological sensitivity (Sensitivity) within the shipping network, and the adaptive capacity (Adaptive Capacity) of its host country—thereby transcending the limitations of conventional single-hazard assessments. Second, based on the compound port risk scores quantified by the GMSC-R model, we introduce a "natural attack" strategy, a climate-informed stress test of the network that sequentially removes port nodes in descending order of climate vulnerability, simulating climate-induced port disruption sequences as an alternative to traditional purely topological attack methods. The core assumption is that ports most vulnerable to compound climate stressors are the most likely to experience significant functional disruption or failure. Here we show, by comparing the GSN in 2017 and 2021, that climate-driven failure sequences can rival deliberate topological attacks in destructive power, that the critical thresholds of network degradation advanced markedly over this four-year window, and that the stress tests expose hidden high-risk ports: climate risk decouples from centrality (Port Said overtakes top-ranked Singapore in the 2021 ranking), and roughly a quarter of the hundred ports failing earliest under climate-informed stress lie outside the corresponding topology-guided removal set. The overall architecture of the framework is illustrated in Fig. 1.

Fig. 1 Analytical framework for assessing climate-driven vulnerability of the global shipping network



Results

Climate-driven vulnerability of the shipping network

The initial topological structure of the 2017 and 2021 networks provides the baseline for all attack simulations: the GSN comprised 1,255 ports and 45,285 links in 2017 and 1,241 ports and 34,897 links in 2021, with overall connectivity contracting markedly (a 22.9% decline in edges) while clustering among core hub ports intensified; the full baseline characterisation is provided in Supplementary Note 1 and Supplementary Table 1. To evaluate the structural vulnerability of the GSN to climate hazards, we simulated a "natural attack" strategy based on the GMSC-R index: port nodes were sequentially removed in descending order of climate risk, with the dynamic changes in network topological performance continuously monitored. Table 1 presents the changes

in each indicator relative to the initial state following the removal of the most vulnerable 66.7% of port nodes.

Table 1. GMSC-R-based vulnerability indicators for 2017 and 2021 shipping networks.

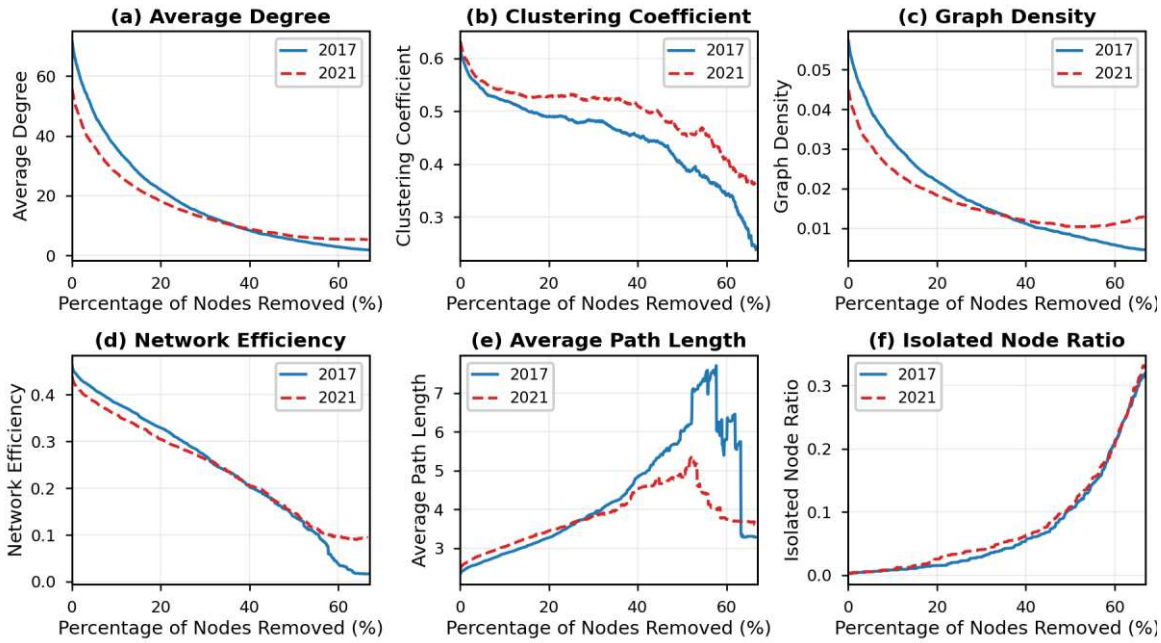
Indicator	2017 Initial	2017 Final	Decline	2021 Initial	2021 Final	Decline
Average degree	72.17	1.92	97.3%	56.24	5.38	90.4%
Avg. clustering coeff.	0.6204	0.2382	61.6%	0.6345	0.3674	42.1%
Graph density	0.0575	0.0046	92.0%	0.0454	0.0131	71.2%
Network efficiency	0.4635	0.0167	96.4%	0.4396	0.0923	79.0%
Avg. path length	2.3333	3.2861	40.8%	2.4641	3.6014	46.2%
Isolated node ratio	0.16%	31.82%	—	0.16%	33.41%	—

The simulation process revealed a strongly nonlinear, front-loaded destructive impact of climate-driven disruptions on the GSN (Fig. 2). In the 2017 simulation, the removal of 66.7% of vulnerable nodes caused network efficiency to decline from an initial 0.4635 to 0.0167, a reduction of 96.4%. In 2021, under the same removal proportion, network efficiency fell from 0.4396 to 0.0923, a reduction of 79.0%; the smaller terminal loss does not indicate greater robustness, as the 2021 network degraded faster in the early stages of the attack and ended more fragmented, but reflects

a weaker overlap between the 2021 climate-risk ranking and the residual connectivity core. Average degree dropped sharply from 72.17 to 1.92 in 2017, a decline of 97.3%, and from 56.24 to 5.38 in 2021, a decline of 90.4%. The average clustering coefficient decreased from 0.6204 to 0.2382 (a decline of 61.6%) in 2017, and from 0.6345 to 0.3674 (a decline of 42.1%) in 2021. Graph density fell from 0.0575 to 0.0046 (a decline of 92.0%) in 2017, and from 0.0454 to 0.0131 (a decline of 71.2%) in 2021. Average path length increased from 2.3333 to 3.2861 (an increase of 40.8%) in 2017, and from 2.4641 to 3.6014 (an increase of 46.2%) in 2021. The proportion of isolated nodes surged from near zero to 31.82% in 2017 and 33.41% in 2021 by the end of the attack.

Further analysis of critical threshold behaviour during the attack process reveals that the network's structural resilience is eroding rapidly. In 2017, the first substantive 5% decline in network efficiency occurred at approximately 1.4% node removal; by 2021, this critical threshold had advanced to only 1.0% node removal. The threshold marking the onset of large-scale network fragmentation—an isolated node ratio exceeding 1%—also shifted forward, from 13.5% node removal in 2017 to 10.8% in 2021 (Fig. 2).

Fig. 2 Trends in global shipping network characteristic indicators under the GMSC-R natural attack.

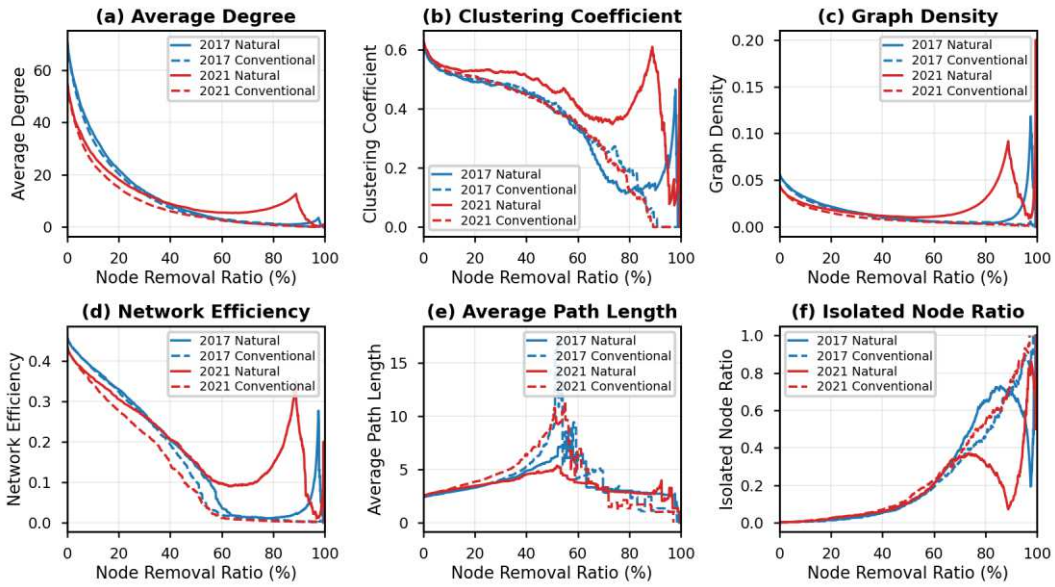


(a) average degree, (b) clustering coefficient, (c) graph density, (d) network efficiency, (e) average path length, and (f) isolated node ratio during the sequential removal of the most vulnerable 66.7% of ports. Solid lines represent 2017; dashed lines represent 2021.

Comparison with conventional topological attacks

To further validate the distinctiveness of the GMSC-R model in identifying network vulnerability, we introduced conventional degree-centrality-based targeted attacks as a benchmark—the classical method in network science that prioritises the removal of the highest-degree nodes. The stability of the network under the two attack strategies can be quantitatively compared by computing the coefficient of variation for each performance indicator (Fig. 3).

Fig. 3 Comparison of network indicators under natural attack versus conventional degree-centrality attack for 2017 and 2021.



(a) average degree, (b) clustering coefficient, (c) graph density, (d) network efficiency, (e) average path length, and (f) isolated node ratio

The network response mechanisms under the two strategies differ fundamentally. For most indicators, the coefficient of variation under conventional topological attacks exceeded that under GMSC-R natural attacks (Fig. 3). Taking network efficiency as an example, the coefficient of variation under conventional attacks (0.616) was 1.2 times that under GMSC-R attacks (0.529) in 2017, and this ratio widened to 1.6 in 2021. After removing 66.7% of nodes, conventional attacks resulted in efficiency losses of 97.2% (2017) and 98.3% (2021); GMSC-R natural attacks produced a comparably devastating 96.4% loss in 2017 but a markedly smaller 79.0% loss in 2021, so that the gap between the climate-driven trajectory and the worst-case topological trajectory widened from 0.8 to 19.5 percentage points. Notably, natural attacks fragmented the network more severely than conventional attacks in both years, isolating 31.8% of nodes versus 27.0% in 2017 and 33.4% versus 30.0% in 2021. The divergence was also evident at the 50% removal level: in 2021, the network maintained an average degree of 6.52 and an efficiency of 0.1485 under GMSC-R attacks, compared with 4.10 and 0.0764 under conventional attacks.

These results demonstrate that removing topologically central nodes indeed inflicts more direct damage to core efficiency, yet such purely topological attack paths often diverge from physically plausible real-world threat patterns. The GMSC-R model reveals a critical asymmetry in how climate risk maps onto network topology: ports of comparable centrality can differ several-fold in compound climate vulnerability. Singapore, for instance, holds the highest betweenness centrality in the 2021 network (0.0856) yet ranks only third by VI, because its high national adaptive capacity (0.79) buffers its exposure, whereas Port Said, with lower centrality (0.0473), rises to second owing to a much weaker adaptive capacity (0.34). Conversely, numerous ports in peripheral or intermediate topological positions, such as Manila and Port-au-Prince, emerge as disproportionately high-risk nodes under climate shocks, because their geographic locations lie deep within extreme-climate-prone zones combined with limited adaptive capacity; it is precisely these ports that drive the heavier fragmentation observed under natural attacks. By integrating the three dimensions of climate exposure, topological sensitivity, and national adaptive capacity, the GMSC-R model more precisely identifies hidden vulnerable nodes that conventional purely topological methods cannot readily capture. This divergence is quantifiable at the level of the attack sequences themselves: only 71% of the first 100 ports removed under the 2021 natural attack rank among the first 100 removed by the degree-based attack (72% in 2017), so roughly one quarter of the earliest climate-driven failures are invisible to purely topological screening (Supplementary Note 2).

Key node identification and spatial distribution

Through the GMSC-R model, we systematically identified and ranked shipping ports facing compound climate risk on a global scale, revealing the complex spatiotemporal dynamics of their

vulnerability. Table 2 lists the top 10 ports by vulnerability index in 2021, together with their 2017 values and changes.

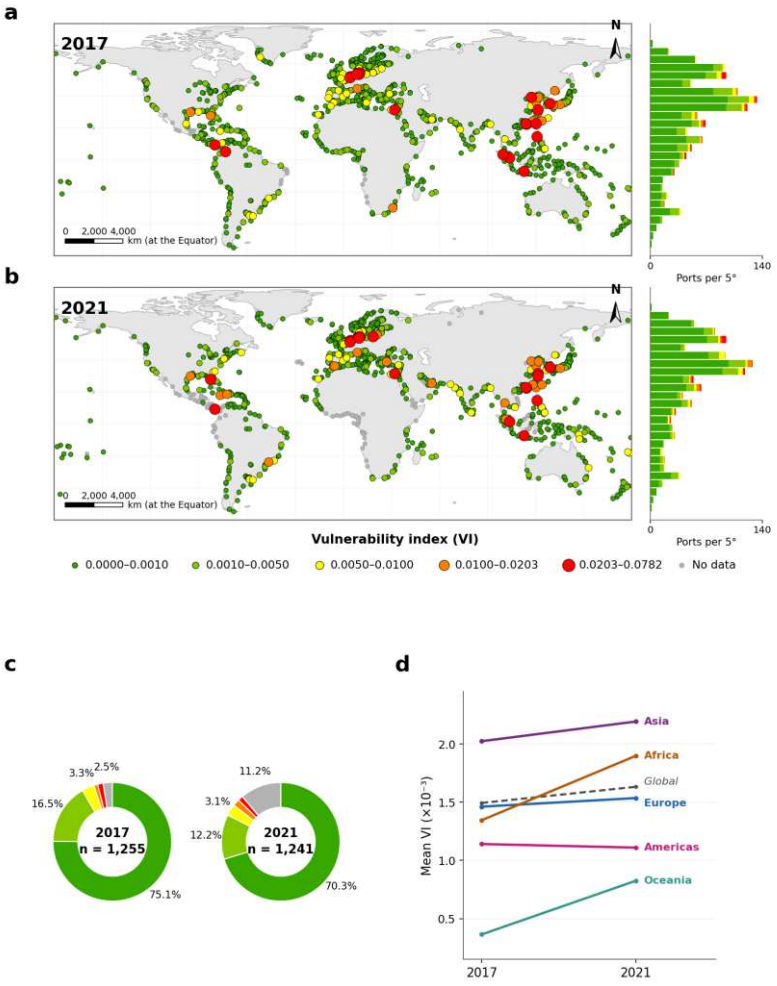
Table 2. Key node identification: top 10 ports by vulnerability index (VI) in 2021.

Port	Country/Region	VI (2017)	VI (2021)	Change	Trend type
Shanghai	China	0.0393	0.0782	+99.3%	Risk sharply escalating
Port Said	Egypt	0.0445	0.0728	+63.5%	Risk markedly rising
Singapore	Singapore	0.0711	0.0654	−8.0%	Sustained extremely high risk
Rotterdam	Netherlands	0.0640	0.0581	−9.2%	Sustained high risk
Hamburg	Germany	0.0439	0.0472	+7.4%	Sustained high risk
Antwerp	Belgium	0.0532	0.0368	−30.8%	Risk receding yet elevated
Ningbo	China	0.0163	0.0366	+124.9%	Risk sharply escalating
Brunsbuttel	Germany	0.0326	0.0352	+7.9%	Sustained high risk
Holtenau (Kiel)	Germany	0.0350	0.0350	+0.1%	Sustained high risk
Hong Kong	China (Hong Kong)	0.0716	0.0332	−53.6%	Risk receding from extreme level

Spatial distribution analysis reveals pronounced uneven geographic clustering of climate vulnerability across the GSN (Fig. 4). In 2021, Asian ports exhibited the highest mean vulnerability index among all continents (0.0022, against a global mean of 0.0016), and Asia hosted the largest number of high-risk–high-vulnerability ports. The 2021 top 10 spans three continents: four ports in Asia, five in Europe, and one in Africa, reflecting the joint imprint of climate exposure, topological centrality, and adaptive capacity. Shanghai (VI = 0.0782) rose to the top of the global ranking with its VI nearly doubling (+99.3%), and Ningbo recorded the largest relative increase among the top 10 (+124.9%). These two exceptionally large increases reflect two compounding

factors. First, their 2017 baselines (VI = 0.0393 and 0.0163, respectively) were low relative to the 2021 leaders, so absolute increases of +0.0390 and +0.0203 translate into a near-doubling or larger percentage change. Second, the tropical-cyclone exposure component of both ports rose sharply in 2021 (from 0.00 to 0.53 and 0.54 on the normalised scale), consistent with the exceptionally destructive typhoon season in the East China Sea that year, most notably Typhoon In-Fa, which made landfall in the Yangtze River Delta in July 2021 and forced the temporary closure of the Shanghai and Ningbo port complexes, followed by Typhoon Chanthu in September, as captured in the IBTrACS records underlying the model. Chinese ports occupied the largest single-economy share of the global top 10: Shanghai, Ningbo, and Hong Kong (VI = 0.0332). Hong Kong, the top-ranked port of 2017 (VI = 0.0716), registered the sharpest decline (−53.6%), driven primarily by the drop in its tropical-cyclone exposure from the exceptionally active 2017 season, which included Super Typhoon Hato, to a single storm within its impact radius in 2021.

Fig. 4 Global spatial distribution of port climate risk.



Port climate risk index (VI) distribution in (a) 2017 (n = 1,255 ports) and (b) 2021 (n = 1,241 ports), shown in an equirectangular projection (60° S–85° N). Circle colour and size jointly encode the VI class; grey circles mark ports without a valid VI in the corresponding year owing to missing tide-gauge records (31 in 2017; 139 in 2021). Marginal bars give the number of ports per 5° latitude band, stacked by VI class. (c) Composition of the port population by VI class. (d) Continental mean VI in 2017 and 2021; the dashed line denotes the global mean (0.0015 in 2017; 0.0016 in 2021).

Decomposition of the hazard drivers for these high-risk nodes reveals a mixed but sea-level-centred structure: six of the 2021 top 10 ports are dominated by sea-level rise, two by tropical

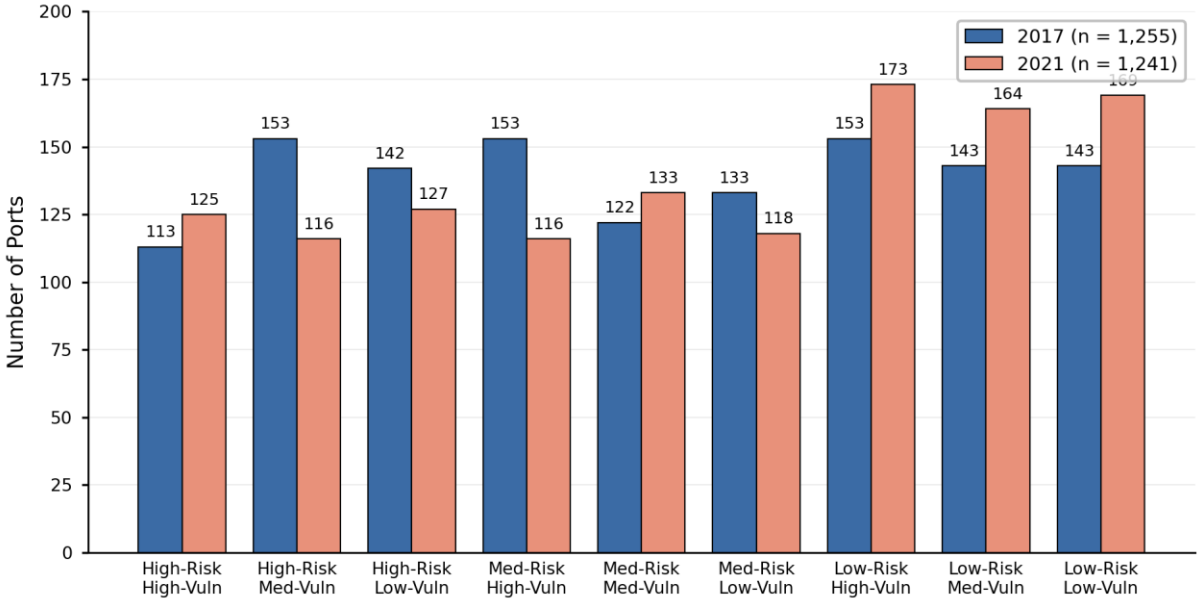
cyclones (Shanghai and Ningbo), and two by sea-ice change (Brunsbuttel and Holtenau). Dominant risk-type statistics corroborate this pattern: among the 125 ports in the high-risk–high-vulnerability core zone in 2021, sea-level-dominated ports accounted for 64.0%, followed by 27.2% dominated by sea-ice change and 8.8% by tropical cyclones.

High-latitude sea-ice-driven risk is equally significant[52,53]. Brunsbuttel (VI = 0.0352, +7.9%) and Holtenau (VI = 0.0350), the two entrances of the Kiel Canal linking the North Sea and the Baltic, ranked among the global top 10 owing to persistently high sea-ice exposure along Baltic approaches (normalised sea-ice components of 0.60 and 0.68), and the number of sea-ice-dominated ports in the core zone rose from 22 in 2017 to 34 in 2021. Furthermore, the trajectory of Port-au-Prince, Haiti—whose VI rose more than tenfold, from 0.0011 to 0.0140, carrying it into the core zone—reveals another dimension: although its climate exposure (0.84) is not the highest globally, its national adaptive capacity (0.22), among the lowest in the entire network, acts as the critical shortfall amplifying systemic vulnerability, allowing the renewed tropical-cyclone exposure of 2021, when Tropical Storm Grace tracked across Haiti in August, to propagate almost unbuffered into its risk index.

Climate risk–topological vulnerability coupling types

To investigate the coupling relationship between port climate exposure and network topological vulnerability, we applied the tertile method to classify all ports into low, medium, and high categories along two dimensions: climate exposure (E) and topological sensitivity (S). This yielded nine risk–vulnerability coupling types. Fig. 5 presents the distribution of ports across the nine coupling types for 2017 and 2021.

Fig. 5 Distribution of ports across climate risk–topological vulnerability coupling types in 2017 and 2021.



Grouped bars show the number of ports in each of the nine coupling types, defined by tertile classification of climate exposure (risk level) and topological sensitivity (vulnerability level); n = 1,255 (2017) and 1,241 (2021).

Comparison of the coupling matrices between the two years reveals structural changes in the risk–vulnerability landscape of the GSN [54]. The most critical shift is the expansion of the high-risk–high-vulnerability core zone: ports in this category increased from 113 in 2017 to 125 in 2021, an increase of 10.6%. Concurrently, the divergence between risk and network vulnerability deepened: low-risk–high-vulnerability ports grew from 153 to 173 and low-risk–medium-vulnerability ports from 143 to 164, while high-risk–medium-vulnerability ports declined from 153 to 116. This mismatch reveals two distinct risk pathways. Some ports, despite being located in high climate exposure zones, exhibit a degree of structural resilience owing to their relatively peripheral topological positions or higher national adaptive capacity. Conversely, another

category of ports, although facing lower direct physical climate risk, are uniquely positioned to transmit even mild climate perturbations into network-wide impacts because of their irreplaceable hub functions within the shipping network.

Dominant risk types in the core zone

To investigate the differentiated influence mechanisms of various climate drivers on port risk, we identified the dominant risk type for each port by comparing the normalised risk indices across the three exposure components: sea-level rise, sea-ice change, and tropical cyclone activity, with the highest-scoring component designated as the dominant type. From a global perspective, sea-level rise remains the most widespread chronic climate threat, with the number of ports it dominates increasing from 1,071 in 2017 to 1,112 in 2021 (85.3% and 89.6% of all classified ports, respectively). Within the high-risk–high-vulnerability core zone, the most systemically destructive segment, sea-level rise likewise dominates, but the internal driver composition shifted markedly between the two years (Table 3).

Table 3. Internal dominant risk structure within the high-risk–high-vulnerability core zone.

Year	Dominant risk type	Port count	Share	Representative ports
2017	Typhoon-dominated	26	23.0%	Hong Kong, Shenzhen, Guangzhou
2017	Sea-level-dominated	65	57.5%	Antwerp, Hamburg, Manila
2017	Sea-ice-dominated	22	19.5%	Holtenau (Kiel), Dalian, Vladivostok
2017	Total	113	100%	—
2021	Typhoon-dominated	11	8.8%	Shanghai, Ningbo, Yokohama
2021	Sea-level-dominated	80	64.0%	Hamburg, Hong Kong, St Petersburg
2021	Sea-ice-dominated	34	27.2%	Brunsbuttel, Holtenau (Kiel), Gdansk

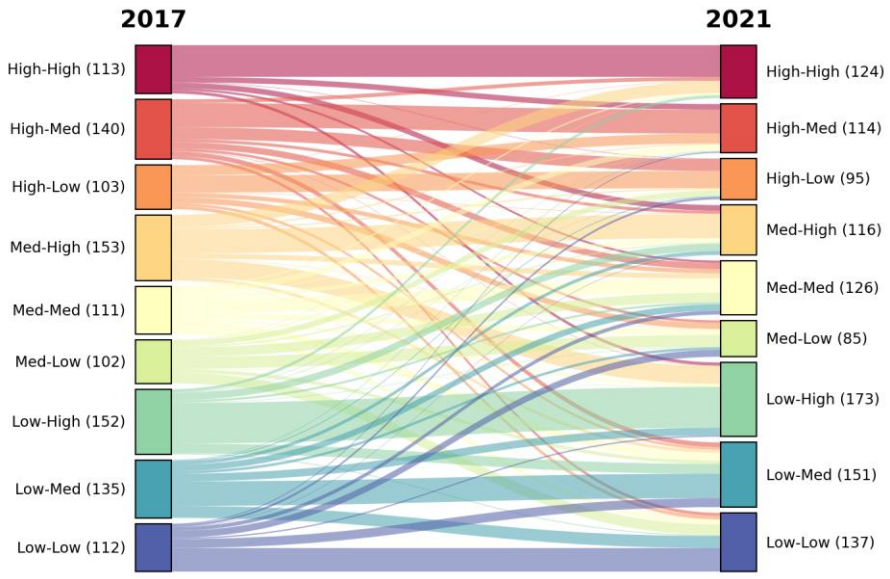
2021	Total	125	100%	—

The data demonstrate that sea-level rise is the dominant driving force at both scales: it accounted for the majority of core-zone ports in both years, and its share rose from 57.5% to 64.0%. This shift reflects the gradual manifestation of sea-level rise accumulation effects, which are progressively pushing ports that were previously in the medium–low risk range into high-risk territory. Equally notable is the near-doubling of the sea-ice-dominated share within the core zone, from 19.5% to 27.2%, concentrated along Baltic and other high-latitude approaches, whereas the typhoon-dominated share contracted from 23.0% to 8.8%, mirroring the strong interannual variability of tropical-cyclone exposure between the two snapshot years.

Spatiotemporal evolution of coupling types

From 2017 to 2021, the evolution of climate risk–vulnerability coupling types exhibited pronounced spatiotemporal heterogeneity, with distinctly different trajectories across continents (Fig. 6). During this period, 126 ports underwent a fundamental shift in their dominant risk type, and 627 of the 1,121 ports present in both networks changed their coupling type.

Fig. 6 Transitions of climate risk–vulnerability coupling types between 2017 and 2021.



Alluvial diagram of port transitions among the nine climate risk–topological vulnerability coupling types from 2017 (left) to 2021 (right); each flow represents a group of ports sharing the same coupling-type trajectory over the period (n = 1,121 ports present in both networks).

In Asia, the risk polarisation trend was most pronounced. The number of high-risk–high-vulnerability ports rose from 36 to 46, contributing the largest share of global core-zone expansion, while high-risk–medium-vulnerability ports increased from 41 to 59. Concurrently, low-risk–low-vulnerability ports decreased from 45 to 29.

The Americas displayed a distinctly different evolutionary pattern. While the high-risk–high-vulnerability count remained marginal (7 in 2017 and 6 in 2021), the dominant movement was out of the medium-risk column: medium-risk–high-vulnerability ports collapsed from 35 to 4, while low-risk–high-vulnerability ports surged from 19 to 48 and low-risk–medium-vulnerability ports rose from 17 to 30. This indicates a structural shift in the risk pattern of the Americas' shipping network: the direct physical threat of climate exposure has relatively diminished, while endogenous deficiencies in network topology are emerging as the more prominent hazard factor.

In Europe, the coupling evolution exhibited a comparatively positive resilience restructuring pattern. The mean vulnerability index of European ports (0.0016) remained well below Asia's (0.0022) in 2021. High-risk–medium-vulnerability ports fell sharply from 69 to 28, and rather than sliding toward the high-vulnerability zone, ports shifted concentratively toward the low-risk column: low-risk–medium-vulnerability ports rose from 25 to 42 and low-risk–low-vulnerability ports from 17 to 34, while the high-risk–high-vulnerability count remained essentially stable (44 to 42).

Discussion

The core contribution of this study lies in providing a systematic assessment framework that transcends conventional topological analysis. By integrating the GMSC-R model—encompassing sea-level variability, sea-ice change, and tropical cyclone activity—with a "natural attack" strategy grounded in physical hazard mechanisms, we quantitatively assessed the systemic risk[54] of the global shipping network under climate change. The GSN exhibits sharply amplified sensitivity to climate-driven port disruptions, and this vulnerability is not randomly distributed but intimately linked to the physical reality of port exposure to specific climate hazards.

The most striking finding is the front-loaded, nonlinear character of climate impacts on network performance and the measurable erosion of early-stage resilience over a mere four-year period. Under the natural attack scenario that removes the most vulnerable 66.7% of ports, network efficiency collapses almost entirely in both years, with losses of 96.4% in 2017 and 79.0% in 2021, while the onset thresholds of degradation advanced from 1.4% to 1.0% of nodes removed for efficiency loss and from 13.5% to 10.8% for large-scale fragmentation. The 22.9% contraction in edges, the 33.41% terminal isolated node ratio, and the earlier critical thresholds in 2021 confirm

that the network is becoming sparser and more fragile. These results suggest that the resilience of the GSN is not declining linearly but may be approaching a critical threshold—a phenomenon consistent with critical transition behaviour widely observed in complex systems[55] and closely aligned with the abrupt cascading collapse characteristics identified in interdependent networks[56,57].

Our findings reveal that sea-level rise constitutes the dominant driving force of GSN climate vulnerability at both global and core-zone scales, with sea-ice change and tropical cyclones exerting differentiated, regionally concentrated roles. Globally, sea-level rise is the most pervasive threat, dominating 89.6% of port risk in 2021—a finding consistent with the early global assessment of port city climate exposure by Nicholls, Hanson, et al.[58]. Within the systemically critical high-risk–high-vulnerability zone its dominance is equally clear, rising from 57.5% to 64.0% of ports between 2017 and 2021, indicating that the long-term cumulative effect of sea-level rise is gradually becoming manifest. Tropical cyclones, by contrast, act as a volatile, high-impact amplifier concentrated in East and Southeast Asia and the Caribbean: the 2021 surges of Shanghai (+99.3%) and Ningbo (+124.9%) were driven by the In-Fa and Chanthu landfalls of that season, reflecting the real-world impacts of the increasing tropical cyclone intensity reported by Knutson et al.[59], Kossin et al.[60], and Murakami et al.[51]. This risk landscape exhibits pronounced spatiotemporal heterogeneity: from 2017 to 2021, the dominant risk type shifted for 126 ports, 83 of which transitioned from typhoon-dominated to sea-level-dominated, while the sea-ice-dominated share of the core zone nearly doubled from 19.5% to 27.2%. Regionally, evolutionary pathways also differed markedly: Asia's high-risk–high-vulnerability ports rose from 36 to 46, remaining the epicentre of global vulnerability intensification; the Americas underwent a structural shift—medium-risk–high-vulnerability ports collapsed while low-risk–high-vulnerability ports

increased significantly, indicating that network structural deficiencies have become a new hazard factor for the region; Europe, by contrast, exhibited a comparatively positive resilience restructuring, underpinned by its stable topological architecture and high national adaptive capacity. These regionally differentiated evolutionary pathways echo the substantial geographic disparities in port adaptive capacity highlighted by Becker et al.[46], and further demonstrate that static, single-dimensional risk assessment can no longer meet the demands of global supply chain risk management; a shift toward dynamic, coupled, and region-specific governance frameworks is imperative.

The comparison with conventional degree-centrality-based attacks highlights the unique value of our framework. Conventional attacks inflict more severe damage to core efficiency[40,42], but this does not reflect real-world climate threat patterns. Our natural attack strategy shows that climate-driven failure sequences can approach the worst-case deliberate attack in destructive power—within 0.8 percentage points of it in 2017—while fragmenting the network periphery even more severely than deliberate attacks in both years, and it identifies hidden high-risk nodes whose compound vulnerability far exceeds what their topological position alone would suggest. Within the interdependent network framework, such nodes, once disrupted, can likewise trigger large-scale cascading collapse[43,57]. These nodes represent weak links that traditional methods readily overlook, yet they may become critical rupture points for global supply chains under climate change shocks.

Several limitations should be acknowledged[61,62]. The GMSC-R model relies on currently available global-scale data, and its spatial resolution has room for further improvement. In particular, quality-controlled global sea-level observations had not yet been updated through 2025 at the time of analysis, which constrains the comparison to the 2017 and 2021 networks; as the

2025 records are released, we will extend the framework to this most recent time point to better observe how climate change is reshaping the vulnerability of the global shipping network. The natural attack simulation simplifies the dynamic processes of port failure and recovery, without fully accounting for network self-adaptation. Furthermore, this study focuses on network structural losses and has not yet directly quantified the economic consequences[39]. Future research should integrate higher-resolution regional climate projections, develop more dynamic network evolution models, and couple economic loss assessment modules to achieve a more comprehensive understanding of GSN vulnerability. Robustness checks show that the main findings (the rising global mean VI, the reshuffled top ranking, and the dominance of sea-level rise in the core zone) are insensitive to the hazard-weighting scheme, the aggregation form, the centrality metric, and the classification thresholds, although near-ties leave the identity of the single top-ranked port sensitive at the margin (Supplementary Note 2).

In conclusion, this study demonstrates that climate change poses an intensifying, nonlinear systemic threat to the global shipping network. The high-risk–high-vulnerability ports concentrated in Asia and Europe—driven by pervasive and accumulating sea-level rise, compounded by episodic tropical-cyclone extremes and expanding sea-ice-related exposure—should be prioritised for adaptive infrastructure investment[63,64]. Our integrated assessment framework provides a scientific foundation for climate-adaptive port planning, supply chain resilience enhancement, and coordinated international efforts[65] to address the challenges that climate change poses to the global trade system.

Methods

Theoretical framework

The theoretical core of this study is the Global Maritime Shipping Climate Risk (GMSC-R) model. The framework first integrates geospatial attributes with complex network physical properties to characterise the traditional locational factors of ports. On this basis, spatial agglomeration levels, port hinterland relationships, and historical typhoon frequency and intensity data are combined as inputs to the GMSC-R model. The model focuses on three key climate risk dimensions for vulnerability assessment: sea-level variability, primarily using tide-gauge water-level data at port breakwaters; sea-ice change, focusing on sea-ice concentration and extent indicators; and tropical cyclone activity, further analysing historical typhoon frequency and intensity. The model outputs then support two interlinked analytical modules—risk propagation analysis and network vulnerability propagation computation—designed to reveal the transmission mechanisms of climate risk through the complex maritime transport system[35,45] and to identify uniquely vulnerable nodes within it. The overall architecture of the framework is illustrated in Fig. 1.

Data acquisition and processing

Global Shipping Network (GSN) data. The GSN was constructed using Automatic Identification System (AIS) data from Alphaliner (https://www.alphaliner.com) for 2017 and 2021. AIS data provide real-time streams of vessel position and identity information and have been widely used to reconstruct shipping networks[66]. In this network representation, ports serve as nodes, and the existence of direct shipping routes derived from vessel movements between ports during the specified period constitutes edges. Consistent with common practice in large-scale topological

analyses focusing on connectivity patterns[67,68], the network is treated as undirected and unweighted.

Typhoon data. Historical track and intensity data for global tropical cyclones were obtained from the International Best Track Archive for Climate Stewardship (IBTrACS), maintained by the National Centers for Environmental Information (NCEI) of the National Oceanic and Atmospheric Administration (NOAA) (https://www.ncei.noaa.gov/products/international-best-track-archive). We used the comprehensive dataset provided in CSV format, extracting relevant records covering 2017 and 2021.

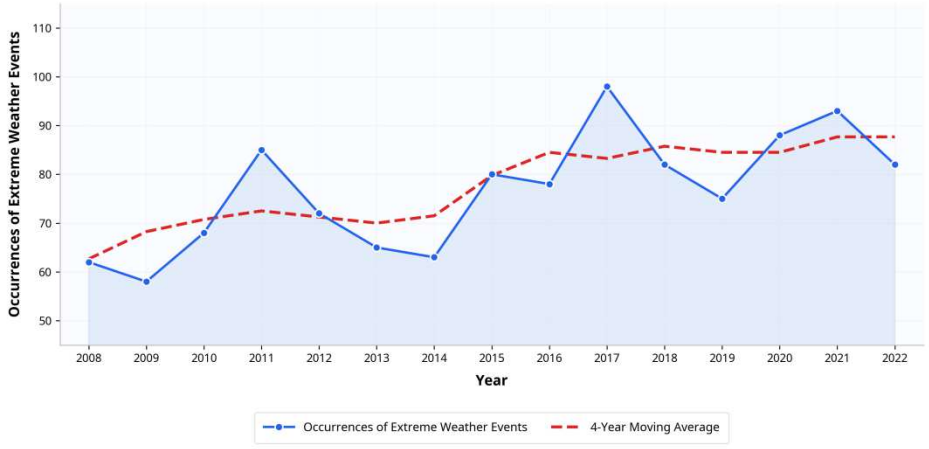
Sea-level variability data. Sea-level data were obtained from the Permanent Service for Mean Sea Level (PSMSL) global database (https://psmsl.org). Tide-gauge records from all monitoring stations were matched to the nearest port by latitude and longitude, yielding port-level sea-level variability data.

Sea-ice change data. Sea-ice data were primarily sourced from the National Snow and Ice Data Center (NSIDC). Sea-ice concentration: global gridded monthly mean sea-ice concentration data were extracted from the NOAA/NSIDC Climate Data Record of Passive Microwave Sea Ice Concentration, Version 4 (dataset identifier: G02202; https://nsidc.org/data/g02202); monthly mean sea-ice concentration data for five Antarctic sub-regions were also computed from this dataset. Sea-ice extent and area: monthly hemispheric sea-ice extent and area data for the Arctic and Antarctic were obtained from the Sea Ice Index, Version 3 (dataset identifier: G02135; https://nsidc.org/data/g02135).

Climate periodicity and year selection. Analysis of NOAA observational data demonstrated that extreme natural events exhibit significant periodicity, and this periodicity is consistent with the approximate four-year cycle of the El Niño–Southern Oscillation (ENSO)[69]. The ENSO-driven

periodicity of extreme events and its implications have been further analysed by IPCC (2021). The years 2017 and 2021, each representing the highest extreme-event day counts within their respective four-year cycles, further corroborate this periodic pattern (Fig. 7). Accordingly, we selected 2017 and 2021 as the analysis years with a four-year cycle interval. This choice captures different types of extreme climate events across different periods and their impacts on the GSN, while the shipping data for both years possess good representativeness, facilitating comparative analysis and trend observation. All climate data were processed to align spatially with port locations and temporally with the network years (2017 and 2021).

Fig. 7 Periodicity of extreme natural events and the selection of analysis years.



Annual count of extreme natural events showing the approximate four-year ENSO-related cycle. The years 2017 and 2021, selected for this study, each represent the highest extreme-event day counts within their respective four-year cycles.

GMSC-R model: port climate risk quantification

To systematically quantify the compound risk level of each port node in the global shipping network under multiple climate stressors, we constructed the Global Maritime Shipping Climate Risk (GMSC-R) model. This model transcends the limitations of conventional single-hazard

climate assessments by integrating the physical climate exposure (E) faced by a port, its topological sensitivity (S) within the shipping network, and the adaptive capacity (AC) of its host country. For any port p in a given year t, the climate risk index VI(p,t) is defined as:

$$VI(p,t) = \frac{E(p,t) \times S(p,t)}{AC(p,t)} \quad (1)$$

where VI(p,t) represents the climate risk index of port p in year t within the GSN; E(p,t) represents the external climate exposure faced by port p in year t; S(p,t) represents the topological sensitivity of port p to climate shocks in year t; and AC(p,t) represents the capacity of port p's host country to cope with, recover from, and adapt to climate hazards in year t. The robustness of the VI construction to the hazard-weighting scheme, the aggregation form, the choice of centrality metric, and the classification thresholds is assessed in Supplementary Note 2. Quantification of climate exposure E(p,t). This study focuses on three core climate hazards that exert direct destructive force on port infrastructure and shipping activities: sea-level rise, sea-ice change, and tropical cyclone activity. The total climate exposure E(p,t) is the linear sum of the three hazard exposure components:

$$E(p,t) = E_SL(p,t) + E_SI(p,t) + E_TC(p,t) \quad (2)$$

The specific calculation and normalisation of each exposure component are as follows:

Sea-level exposure E_SL(p,t):

$$E_SL(p,t) = \frac{SL(p,t) - SL_{\min}}{SL_{\max} - SL_{\min}} \quad (3)$$

where SL(p,t) is the absolute sea-level rise value for the region of port p in year t, normalised via min–max scaling to eliminate dimensionality effects.

Sea-ice exposure E_SI(p,t):

$$E_SI(p,t) = \frac{SI_{area}(p,t)}{SI_{area,max}} + \frac{SI_{density}(p,t)}{SI_{density,max}} \quad (4)$$

where SI_area(p,t) and SI_density(p,t) are variables quantifying the sea-ice area and density affecting port p or its access routes in year t, both normalised by their respective maximum values.

Typhoon exposure E_TC(p,t):

$$E_TC(p,t) = \frac{1}{2}\left(\frac{TF_{freq}(p,t)}{TF_{freq,max}} + \frac{TF_{int}(p,t)}{TF_{int,max}}\right) (5)$$

where TF_freq(p,t) and TF_int(p,t) quantify the typhoon occurrence frequency and mean intensity affecting port p in year t, also normalised by extreme-value scaling.

Quantification of topological sensitivity S(p,t). The topological sensitivity of port p is measured by its normalised betweenness centrality in the year-t shipping network:

$$S(p,t) = \frac{2}{(N-1)(N-2)} \sum_{i \neq p \neq j} \frac{\sigma_{ij}(p)}{\sigma_{ij}} (6)$$

where σ_ij is the number of shortest paths between ports i and j in the year-t network, σ_ij(p) is the number of those paths that pass through port p, and N is the number of ports; the normalisation confines S(p,t) to the interval [0, 1]. Betweenness centrality is computed separately on the 2017 and 2021 networks, so the sensitivity term is year-specific. A port with high betweenness centrality mediates a disproportionate share of shortest transport paths, and its climate-induced failure therefore disrupts connectivity well beyond its own throughput.

Quantification of adaptive capacity AC(p,t). The adaptive capacity of port p is proxied by the Readiness score of its host country in the Notre Dame Global Adaptation Initiative (ND-GAIN) Country Index for year t. The Readiness score, reported on a 0–1 scale, aggregates economic, governance and social indicators of a country's capacity to mobilise and deploy adaptation investment; all ports in the same country share the country-level value, and no further normalisation is applied. Because AC(p,t) enters the denominator of the vulnerability index, higher national readiness proportionally discounts the compound risk of a port, whereas the same exposure and network position translate into greater risk for ports in countries with low readiness.

Network vulnerability metrics

To quantify the impact of natural attacks on GSN structure and function, the following standard network metrics were computed [67,70] before and after the removal of vulnerable nodes:

Average degree ($\bar{k}$): the mean number of connections per node; a decrease indicates loss of connectivity.

$$k = \frac{2E}{N} (7)$$

where E is the number of edges and N is the number of nodes.

Average clustering coefficient (C): a measure of the extent to which nodes tend to cluster together, computed as the mean of the local clustering coefficients across all nodes.

$$C = \frac{C_i_1 + C_i_2 + \ldots + C_i_N}{\mathrm{N}} (8)$$

where C_1, C_2, ..., C_N are the local clustering coefficients of nodes 1 through N, and N is the total number of nodes in the network.

Average path length (L): the mean shortest distance between all reachable node pairs, typically computed within the largest connected component; an increase indicates reduced transport efficiency.

$$L = \frac{1}{N(N-1)} \sum_{i \neq j} d\,(i,j) (9)$$

where d(i, j) is the shortest path distance between nodes i and j [67].

Network efficiency (Eff): a measure of the efficiency with which information or goods are transported across the network, related to the inverse of the shortest path length [38]; a decrease indicates overall degradation of network performance.

$$Eff = \frac{1}{N(N-1)} \sum_{i \neq j} \frac{1}{d(i,j)} (10)$$

Isolated node ratio (R_isolated): the proportion of nodes with zero connections.

$$\mathrm{Ratio}_{\mathrm{isolated}} = \frac{\mathrm{N}_{\mathrm{k=0}}}{\mathrm{N}} (11)$$

where N_{k=0} is the number of nodes with degree zero.

Network density (ρ): the ratio of existing edges to the maximum possible number of edges, reflecting the overall level of connectivity.

$$\rho = \frac{E}{\frac{N(N-1)}{2}} (12)$$

Natural attack sequence construction and scenario simulation

To assess the vulnerability of the GSN under climate change, we employed a natural-risk-based attack strategy. Unlike conventional purely topological attacks, this strategy simulates disruption scenarios driven by climate vulnerability with a stronger physical basis. The simulation process

was conducted for 2017 and 2021, integrating three components: network construction, vulnerability assessment, and attack simulation.

(1) Construct initial network: the initial GSN for each year was built using AIS data, with ports as nodes and routes as edges.

(2) Compute initial indicators: the initial GSN network indicators (as shown in Supplementary Table 1) were calculated—including average degree, average clustering coefficient, graph density, network efficiency, average path length, and isolated node ratio—to establish the baseline.

(3) Quantify port risk: the compound climate vulnerability score VI(p,t) for each port was computed using the corresponding climate data and the GMSC-R model (Eqs. 1–6).

(4) Construct the attack sequence: all ports were ranked in descending order of their computed VI(p,t) scores. The attack sequence sequentially removes the top two-thirds (approximately 66.7%) of the most vulnerable ports from the network. The core assumption is that ports most vulnerable to compound climate stressors are the most likely to experience significant functional disruption or failure.

(5) Simulate attack and assess: after sequentially removing the specified proportion of nodes, the network indicators of the remaining network were computed. The choice to remove the top two-thirds of nodes represents a severe disruption scenario designed to probe the network's response under extreme, climate-induced stress, allowing exploration of network behaviour near potential tipping points. This is consistent with methodologies used in similar network robustness studies evaluating significant stress impacts [71,72].

(6) Analyse vulnerability: by comparing the pre- and post-attack changes in network indicators (as shown in Table 1), the vulnerability of the network was quantified and the degree of structural and

functional degradation was assessed. Through this integrated workflow, we systematically evaluated the potential impacts of climate-risk-based disruptions on GSN performance.

Data availability

The AIS-derived global shipping network data that support the findings of this study are available from Alphaliner but restrictions apply to the availability of these data, which were used under licence for the current study and are not publicly available. Typhoon track data are publicly available from the IBTrACS database maintained by NOAA NCEI (https://www.ncei.noaa.gov/products/international-best-track-archive). Sea-level data are publicly available from the Permanent Service for Mean Sea Level (PSMSL, https://psmsl.org). Sea-ice concentration data are publicly available from the NOAA/NSIDC Climate Data Record (G02202, https://nsidc.org/data/g02202), and sea-ice extent and area data from the Sea Ice Index Version 3 (G02135, https://nsidc.org/data/g02135). National adaptive-capacity data are publicly available from the Notre Dame Global Adaptation Initiative (ND-GAIN) Country Index (https://gain.nd.edu/our-work/country-index/). Derived data supporting the findings of this study, including the port climate risk index values and network metrics, are available from the corresponding author upon reasonable request.

Code availability

The Python code used for network construction, GMSC-R model computation, and the attack simulations is available from the corresponding author upon reasonable request.

Author contributions

Competing interests

The authors declare no competing interests.

References

[1] UNCTAD. (2024). Review of Maritime Transport 2024. United Nations.

[2] Liu, J., Wu, J., & Gong, Y. (2023). Maritime supply chain resilience: From concept to practice. Computers & Industrial Engineering, 182, 109366.

[3] IPCC. (2021). Climate Change 2021: The Physical Science Basis. Cambridge University Press.

[4] Verschuur, J., Koks, E. E., Li, S., & Hall, J. W. (2023). Multi-hazard risk to global port infrastructure and resulting trade and logistics losses. Communications Earth & Environment, 4, 5.

[5] Fernandez-Perez, A., Lara, J. L., Lucio, D., & Losada, I. J. (2024). Compound climate change risk analysis for port infrastructures. Coastal Engineering, 193, 104560.

[6] Izaguirre, C., Losada, I. J., Camus, P., Vigh, J. L., & Stenek, V. (2021). Climate change risk to global port operations. Nature Climate Change, 11(1), 14-20.

[7] Hallegatte, S., Green, C., Nicholls, R. J., & Corfee-Morlot, J. (2013). Future flood losses in major coastal cities. Nature Climate Change, 3(9), 802-806.

[8] Nicholls, R. J., Hanson, S. E., Lowe, J. A., Slangen, A. B. A., Wahl, T., Hinkel, J., & Long, A. J. (2021). Integrating new sea-level scenarios into coastal risk and adaptation assessments: An ongoing process. WIREs Climate Change, 12(3), e706.

[9] Zhao, P., Li, Y., Zhang, C., Kang, T., He, Z., Huang, G., ... & Kong, W. (2025). Arctic Sea Route access reshapes global shipping carbon emissions. Nature Communications, 16(1), 8431.

[10] Melia, N., Haines, K., & Hawkins, E. (2016). Sea ice decline and 21st century trans-Arctic shipping routes. Geophysical Research Letters, 43(18), 9720-9728.

[11] Aksenov, Y., Popova, E. E., Yool, A., Nurser, A. J. G., Williams, T. D., Bertino, L., & Bergh, J. (2017). On the future navigability of Arctic sea routes. Marine Policy, 75, 300-317.

[12] Khon, V. C., Mokhov, I. I., Latif, M., Semenov, V. A., & Park, W. (2017). Transit navigation through Northern Sea Route. Environmental Research Letters, 12(2), 024010.

[13] Liu, M., & Kronbak, J. (2010). The potential economic viability of using the Northern Sea Route. Journal of Transport Geography, 18(3), 434-444.

[14] Henke, M. T., Miesse, T., de Souza de Lima, A., Ferreira, C., Ravens, T., & Pundt, R. (2024). Evolving Arctic maritime hazards: Declining sea ice and rising waves in the Northwest Passage. PNAS, 121(29), e2400355121.

[15] Pizzolato, L., Howell, S. E. L., Derksen, C., Dawson, J., & Copland, L. (2014). Changing sea ice conditions and marine transportation activity in Canadian Arctic waters between 1990 and 2012. Climatic Change, 123(2), 161-173.

[16] Wei, T., Dong, W. J., Chen, Y. L., & Qi, W. (2025). Asymmetric response of Arctic sea ice and navigation to carbon emissions. Advances in Climate Change Research, 16(6), 1141-1149.

[17] World Economic Forum. (2024). The Global Risks Report 2024 (19th ed.). WEF.

[18] Wang, H., Gao, L., Zhu, L., Zhang, L., & Wu, J. (2024). Changes in the typhoon intensity under a warming climate: A numerical study of typhoon Mangkhut. Journal of Climate, 37(14), 3703-3722.

[19] Shen, Z., Xu, X., Li, J., & Wang, S. (2019). Vulnerability of the maritime network to tropical cyclones in the Northwest Pacific and the Northern Indian Ocean. Sustainability, 11(21), 6176.

[20] Ali, I., Arslan, A., Tarba, S., & Mainela, T. (2023). Supply chain resilience to climate change inflicted extreme events in agri-food industry: The role of social capital and network complexity. International Journal of Production Economics, 264, 108968.

[21] Verschuur, J., Lumma, J., & Hall, J. W. (2025). Systemic impacts of disruptions at maritime chokepoints. Nature Communications, 16(1), 10421.

[22] Bai, X., Ma, Z., & Zhou, Y. (2023). Data-driven static and dynamic resilience assessment of the global liner shipping network. Transportation Research Part E, 170, 103016.

[23] Becker, A., Inoue, S., Fischer, M., & Schwegler, B. (2012). Climate change impacts on international seaports. Climatic Change, 110(1-2), 5-29.

[24] Becker, A. (2020). Climate change impacts to ports and maritime supply chains. Maritime Policy & Management, 47(7), 849-852.

[25] Ducruet, C. (2020). The geography of maritime networks: A critical review. Journal of Transport Geography, 88, 102824.

[26] Barthelemy, M. (2011). Spatial networks. Physics Reports, 499(1-3), 1-101.

[27] Hu, Y., & Zhu, D. (2009). Empirical analysis of the worldwide maritime transportation network. Physica A, 388(10), 2061-2071.

[28] Kaluza, P., Kolzsch, A., Gastner, M. T., & Blasius, B. (2010). The complex network of global cargo ship movements. Journal of the Royal Society Interface, 7(48), 1093-1103.

[29] Barabasi, A.-L., & Albert, R. (1999). Emergence of scaling in random networks. Science, 286(5439), 509-512.

[30] Watts, D. J., & Strogatz, S. H. (1998). Collective dynamics of 'small-world' networks. Nature, 393(6684), 440-442.

[31] Qin, Y., Guo, J., & Wu, S. (2025). The resilience evolution and dynamic process identification of the global shipping network. Transport Policy, 174, 103851.

[32] Holme, P., & Saramaki, J. (2012). Temporal networks. Physics Reports, 519(3), 97-125.

[33] Barrat, A., Barthelemy, M., Pastor-Satorras, R., & Vespignani, A. (2004). The architecture of complex weighted networks. PNAS, 101(11), 3747-3752.

[34] Kivela, M., Arenas, A., Barthelemy, M., Gleeson, J. P., Moreno, Y., & Porter, M. A. (2014). Multilayer networks. Journal of Complex Networks, 2(3), 203-271.

[35] Zhang, M., Huang, T., Guo, Z., & He, Z. (2022). Complex-network-based traffic network analysis and dynamics: A comprehensive review. Physica A, 607, 128063.

[36] Chen, J., Jiang, H., Xu, J., Pang, C., Shi, J., & Tan, Z. (2025). Resilience analysis from the perspective of global container shipping network evolution: Fine-grained modeling based on AIS data. Journal of Transport Geography, 129, 104415.

[37] Viljoen, N. M., & Joubert, J. W. (2016). The vulnerability of the global container shipping network. Physica A, 462, 396-409.

[38] Latora, V., & Marchiori, M. (2001). Efficient behavior of small-world networks. Physical Review Letters, 87(19), 198701.

[39] Faturechi, R., & Miller-Hooks, E. (2015). Measuring the performance of transportation infrastructure systems in disasters. Journal of Infrastructure Systems, 21(1), 04014025.

[40] Albert, R., Jeong, H., & Barabasi, A.-L. (2000). Error and attack tolerance of complex networks. Nature, 406(6794), 378-382.

[41] Holme, P., Kim, B. J., Yoon, C. N., & Han, S. K. (2002). Attack vulnerability of complex networks. Physical Review E, 65(5), 056109.

[42] Callaway, D. S., Newman, M. E. J., Strogatz, S. H., & Watts, D. J. (2000). Network robustness and fragility: Percolation on random graphs. Physical Review Letters, 85(25), 5468-5471.

[43] Motter, A. E., & Lai, Y.-C. (2002). Cascade-based attacks on complex networks. Physical Review E, 66(6), 065102.

[44] Xu, Y., Peng, P., Claramunt, C., Lu, F., & Yan, R. (2024). Cascading failure modelling in global container shipping network using mass vessel trajectory data. Reliability Engineering & System Safety, 249, 110231.

[45] Zhang, D., Tao, J., Wan, C., Huang, L., & Yang, M. (2024). Resilience analysis of maritime transportation networks: A systematic review. Transportation Safety and Environment, 6(4), tdae009.

[46] Becker, A., Acciaro, M., Asariotis, R., Cabrera, E., Cretegny, L., Esteban, M., ... & Velegrakis, A. F. (2013). A note on climate change adaptation for seaports. Climatic Change, 120(4), 683-695.

[47] Becker, A., Ng, A. K. Y., McEvoy, D., & Mullett, J. (2018). Implications of climate change for shipping: Ports and supply chains. WIREs Climate Change, 9(2), e508.

[48] Guo, J., Feng, T., Wang, S., Qin, Y., & Yu, X. (2024). Shipping network vulnerability assessment integrated with geographical locations. Transportation Research Part D, 130, 104166.

[49] Yang, Z., Lau, Y. Y., Poo, M. C. P., Yin, J., & Yang, Z. (2025). Port resilience to climate change in the Greater Bay Area. Transportation Research Part D, 142, 104681.

[50] Jiang, L., Wang, G., Feng, X., Yu, T., & Lei, Z. (2024). Study on cascading failure vulnerability of the 21st-century Maritime Silk Road container shipping network. Journal of Transport Geography, 117, 103891.

[51] Murakami, H., Cooke, W. F., Mizuta, R., Endo, H., Yoshida, K., Wang, S., & Hsu, P.-C. (2024). Robust future projections of global spatial distribution of major tropical cyclones and sea level pressure gradients. Communications Earth & Environment, 5, 479.

[52] Basnayake, V., Duong, T. M., Ranasinghe, R., Almar, R., & Wijnberg, K. M. (2026). A global assessment of coastal vulnerability and dominant contributors. Nature Communications, 17(1), 578.

[53] Rizzo, A., Mattei, G., Dumon Steenssens, L., Anzidei, M., Aucelli, P. P. C., Alberti, T., ... & Mastronuzzi, G. (2025). Methodological advances in sea level rise vulnerability assessment: Implications for sustainable coastal management in a climate change scenario. Ocean & Coastal Management, 268, 107751.

[54] Wang, N., Yuen, K. F., Gao, X., & Nie, Y. (2025). Resilience assessment of global container shipping network via port communities. Transportation Research Part D, 141, 104649.

[55] Scheffer, M., Bascompte, J., Brock, W. A., Brovkin, V., Carpenter, S. R., Dakos, V., ... & Sugihara, G. (2009). Early-warning signals for critical transitions. Nature, 461(7260), 53-59.

[56] Valdez, L. D., Shekhtman, L., La Rocca, C. E., Zhang, X., Buldyrev, S. V., Trunfio, P. A., ... & Havlin, S. (2020). Cascading failures in complex networks. Journal of Complex Networks, 8(2), cnaa013.

[57] Buldyrev, S. V., Parshani, R., Paul, G., Stanley, H. E., & Havlin, S. (2010). Catastrophic cascade of failures in interdependent networks. Nature, 464(7291), 1025-1028.

[58] Nicholls, R. J., Hanson, S. E., Lowe, J. A., Warrick, R. A., Lu, X., & Long, A. J. (2014). Sea-level scenarios for evaluating coastal impacts. WIREs Climate Change, 5(1), 129-150.

[59] Knutson, T., Camargo, S. J., Chan, J. C., Emanuel, K., Ho, C. H., Kossin, J., ... & Wu, L. (2020). Tropical cyclones and climate change assessment: Part II. Bulletin of the American Meteorological Society, 101(3), E303-E322.

[60] Kossin, J. P., Knapp, K. R., Olander, T. L., & Velden, C. S. (2020). Global increase in major tropical cyclone exceedance probability. PNAS, 117(22), 11975-11980.

[61] Panahi, R., Ng, A. K. Y., & Pang, J. (2020). Climate change adaptation in the port industry: A complex of lingering research gaps and uncertainties. Transport Policy, 95, 10-26.

[62] Jenkins, K., Nicholls, R. J., & Sayers, P. (2025). Climate change adaptation in the port industry: Evaluating evidence of implemented adaptation using a national adaptation inventory. Earth's Future, 13(10), e2024EF005841.

[63] Sierra, J. P. (2019). Economic impact of overtopping and adaptation measures in Catalan ports due to sea level rise. Water, 11(7), 1440.

[64] Yang, Y. C., & Ge, Y. E. (2020). Adaptation strategies for port infrastructure and facilities under climate change at the Kaohsiung port. Transport Policy, 97, 232-244.

[65] Leon-Mateos, F., Sartal, A., Lopez-Manuel, L., & Quintas, M. A. (2021). Adapting our sea ports to the challenges of climate change: Development and validation of a Port Resilience Index. Marine Policy, 130, 104573.

[66] Wang, Z., Claramunt, C., & Wang, Y. (2019). Extracting global shipping networks from massive historical Automatic Identification System sensor data: A bottom-up approach. Sensors, 19(15), 3363.

[67] Newman, M. E. J. (2003). The structure and function of complex networks. SIAM Review, 45(2), 167-256.

[68] Garcia Alvarez, N., Adenso-Diaz, B., & Calzada-Infante, L. (2021). Maritime traffic as a complex network: A systematic review. Networks and Spatial Economics, 21(2), 387-417.

[69] Cai, W., Santoso, A., Collins, M., Dewitte, B., Karamperidou, C., Kug, J. S., ... & Zheng, X. T. (2021). Changing El Nino-Southern Oscillation in a warming climate. Nature Reviews Earth & Environment, 2(9), 628-644.

[70] Freeman, L. C. (1977). A set of measures of centrality based on betweenness. Sociometry, 40(1), 35-41.

[71] Smolyak, A., Levy, O., Vodenska, I., Buldyrev, S. V., & Havlin, S. (2020). Mitigation of cascading failures in complex networks. Scientific Reports, 10, 16124.

[72] Cohen, R., Erez, K., ben-Avraham, D., & Havlin, S. (2001). Breakdown of the Internet under intentional attack. Physical Review Letters, 86(16), 3682-3685.

Supplementary Information

Supplementary Note 1 | Initial-state analysis of the global shipping network

Prior to conducting the vulnerability attack simulations reported in the main text, we quantified the initial topological structure of the 2017 and 2021 global shipping networks to establish a baseline for subsequent assessment. The GSN was constructed as an undirected, unweighted network model. Supplementary Table 1 summarises seven key performance indicators for both years.

The overall scale of the GSN remained relatively stable over the four-year period, with the number of nodes declining slightly from 1,255 to 1,241, yet its internal connectivity underwent a dramatic contraction. The number of edges decreased sharply from 45,285 to 34,897—a decline of 22.9%—directly driving average degree down from 72.17 to 56.24 (Supplementary Table 1). Notably, the average clustering coefficient exhibited a counter-trend increase of 2.3%, rising from 0.6204 to 0.6345. This combination of declining density and rising clustering reveals that the network is evolving toward a more extreme core–periphery structure: although overall connectivity has become sparser, local clustering among core hub ports has intensified, forming tighter local subgroups. Concurrently, network efficiency decreased from 0.4635 to 0.4396 (a decline of 5.2%), and average path length increased from 2.3333 to 2.4641 (an increase of 5.6%), jointly indicating that the efficiency of cargo movement through the global network is declining, and the network's buffer capacity against local disruptions has been further compressed.

Supplementary Table 1. Initial network performance indicators for 2017 and 2021.

Indicator	2017	2021	Change (%)
Number of nodes (N)	1,255	1,241	−1.1%

Indicator	2017	2021	Change (%)
Number of edges (E)	45,285	34,897	−22.9%
Average degree	72.17	56.24	−22.1%
Graph density	0.0575	0.0454	−21.2%
Average clustering coefficient	0.6204	0.6345	+2.3%
Network efficiency	0.4635	0.4396	−5.2%
Average path length	2.3333	2.4641	+5.6%
Isolated node ratio	0.16%	0.16%	0.0%

Supplementary Note 2 | Robustness of the GMSC-R vulnerability index construction

This note assesses the robustness of the vulnerability index VI = E × S / AC to the principal construction choices of the GMSC-R model: the weighting of the three hazard components within the exposure term (baseline: equal weights, E = E_SL + E_SI + E_TC), the aggregation form, the centrality metric used for topological sensitivity S (baseline: betweenness centrality), and the tertile thresholds used for the coupling classification. Analyses are restricted to ports with complete records for all three hazard components (n = 1,223 in 2017; n = 1,101 in 2021); agreement with the baseline is measured by the Spearman rank correlation (ρ) of the full VI ranking and by the overlap of the top-10 port sets.

Hazard weighting. We recomputed VI for every weighting E(w) = w_SL E_SL + w_SI E_SI + w_TC E_TC on a simplex grid with step 0.05 (231 weightings per year). Rankings are highly stable: the median ρ is 0.995 (2017) and 0.997 (2021), and ρ exceeds 0.84 and 0.88, respectively, for 95% of weightings; agreement degrades only near single-hazard corners such as w_TC = 1,

which abandon the multi-hazard premise of the model. Within the interior region in which every hazard retains material weight (each $w \geq 0.15$; 68 weightings), $\rho \geq 0.991$ in 2017 and ≥ 0.995 in 2021 (median 0.999 in both years), and at least 5 (2017) and 7 (2021) of the baseline top-10 ports remain in the top 10 (median 8). The global mean VI is higher in 2021 than in 2017 under all 231 weightings, so the conclusion that network-wide climate risk is rising is independent of the weighting scheme. By contrast, the identity of the single top-ranked port is marginal: Hong Kong and Singapore are separated by less than 1% of VI in 2017, and Shanghai's 2021 lead is typhoon-driven. The baseline leader remains within the top two for 66% (2017) and 74% (2021) of interior weightings, and Port Said remains within the top five for 94% (Supplementary Table 2).

Supplementary Table 2. Sensitivity of the VI ranking to the hazard-weighting scheme.

Weight set	Year	ρ (min)	ρ (median)	Top-10 overlap (min / median)	Baseline leader in top 2 (%)
Full simplex (n = 231)	2017	0.156	0.995	3 / 8	50
Full simplex (n = 231)	2021	0.224	0.997	3 / 7	52
Interior, each $w \geq 0.15$ (n = 68)	2017	0.991	0.999	5 / 8	66
Interior, each $w \geq 0.15$ (n = 68)	2021	0.995	0.999	7 / 8	74

Baseline leader: Hong Kong (2017); Shanghai (2021). The global mean VI is higher in 2021 than in 2017 for all 231 weightings in both the full and interior sets.

Aggregation form. Moving adaptive capacity from the denominator to a multiplicative deficit term, $VI = E \times S \times (1 - AC')$ with AC' the min–max-normalised adaptive capacity, preserves the baseline ranking ($\rho = 0.93$ in 2017 and 0.98 in 2021; top-10 overlap 6 of 10 in both years). A fully compensatory additive index, defined as the sum of the percentile ranks of E, S and (1 − AC), yields a materially different ranking ($\rho = 0.77$ and 0.74), because additive aggregation allows high exposure to compensate for negligible network centrality and vice versa. The multiplicative baseline is therefore a substantive and deliberate modelling choice: it encodes the risk-theoretic requirement that compound risk vanishes when any constituent dimension vanishes, consistent with the geometric aggregation used by established composite risk indices (Supplementary Table 3).

Centrality metric. Substituting degree or eigenvector centrality for betweenness centrality leaves the results essentially unchanged ($\rho = 0.91/0.89$ and 0.87/0.84 for 2017/2021; top-10 overlap 4–7), and both alternatives preserve the 2021 ranking reported in the main text, with Shanghai within the top two and Port Said within the top five. Closeness centrality is the exception ($\rho \approx 0.37$): in a dense small-world network, closeness is nearly uniform across nodes (coefficient of variation 0.14, versus 1.1 for degree and 4.0 for betweenness centrality) and therefore carries almost no discriminating information (Supplementary Table 3).

Supplementary Table 3. Alternative aggregation forms and centrality metrics.

Variant	Year	ρ	Top-10 overlap	Ranking criterion met

AC as deficit multiplier	2017	0.933	6	Yes
AC as deficit multiplier	2021	0.978	6	Yes
Rank-additive	2017	0.767	2	No
Rank-additive	2021	0.738	0	No
S = degree centrality	2017	0.911	5	Yes
S = degree centrality	2021	0.891	7	Yes
S = eigenvector centrality	2017	0.871	4	Yes
S = eigenvector centrality	2021	0.842	5	Yes
S = closeness centrality	2017	0.366	2	No
S = closeness centrality	2021	0.384	0	No

Ranking criterion: Hong Kong within the top 2 (2017); Shanghai within the top 2 and Port Said within the top 5 (2021).

Classification thresholds and attack sequences. Perturbing the tertile thresholds of the coupling classification (to the 30th/70th or 35th/65th percentiles, or to quartiles) changes the size of the high-risk–high-vulnerability core zone (61–126 ports in 2017; 79–144 in 2021) but not its composition: sea-level rise remains the leading dominant hazard under every rule (52.5–59.5% of

the core zone in 2017; 51.9–67.4% in 2021), with sea-ice change ranking second throughout 2021 (Supplementary Table 4). Finally, comparing the attack sequences themselves, only 72% (2017) and 71% (2021) of the first 100 ports removed under the natural attack rank among the first 100 removed under the degree-based attack, confirming that roughly one quarter of the earliest climate-driven failures are invisible to purely topological screening.

Supplementary Table 4. Core-zone composition under alternative classification thresholds.

Threshold rule	Year	Core-zone n	Sea-level (%)	Sea-ice (%)	Typhoon (%)
Tertile (baseline)	2017	113	57.5	19.5	23.0
30th / 70th percentile	2017	92	57.6	19.6	22.8
35th / 65th percentile	2017	126	59.5	17.5	23.0
Quartile	2017	61	52.5	21.3	26.2
Tertile (baseline)	2021	125	64.0	27.2	8.8
30th / 70th percentile	2021	108	59.3	30.6	10.2
35th / 65th percentile	2021	144	67.4	25.0	7.6
Quartile	2021	79	51.9	34.2	13.9

Taken together, these checks indicate that the principal findings of the main text are robust to the construction choices of the GMSC-R model: the rising global mean VI, the near-total efficiency

loss under the natural attack, the reshuffled composition of the top-ranked ports, the dominance of sea-level rise in the core zone, and the divergence between climate-informed and topology-guided failure sequences all persist across the alternatives examined, whereas single-rank identities separated by narrow margins are treated as near-ties.